AIAA 80-0003R

Evaluation of Three-Dimensional Transonic Codes Using New Correlation-Tailored Test Data

B. L. Hinson* and K. P. Burdges†
Lockheed-Georgia Company, Marietta, Ga.

A comprehensive research program was conducted for the specific purpose of acquiring benchmark test data suitable for evaluations of three-dimensional transonic codes. High-quality data were obtained for three advanced technology wings by using a unique test apparatus and by devoting careful attention to details of the experiment. The test apparatus included provisions for removal of the wind tunnel boundary layer and measurements of far-field pressures. The test data were used in preliminary evaluations of three selected transonic computational methods. For these limited evaluations, nonconservative formulations more closely predicted measured pressures than conservative formulations. In addition, full potential solutions were found to be uniformly in better agreement with experiment than small disturbance results.

Nomenclature

AR	= wing aspect ratio, b^2/S
b	= wing span
C	= streamwise local chord of wing
C_L	= lift coefficient
C_p	= pressure coefficient
M	= freestream Mach number
S	= wing planform area
x,y,z	= Cartesian coordinates
α	= angle of attack
η	= span station, $y/(b/2)$
θ	= wing section local incidence angle
λ	= wing taper ratio, C_t/C_r
Λ	= wing sweep angle
τ	= wind tunnel wall porosity
ϕ	= perturbation velocity potential

Subscripts

$c/4$	= quarter chord
M	= measured
r	= wing root
t	= wing tip

Introduction

SINCE the original work of Bailey and Ballhaus[1] in the early 1970s, significant advancements have been made in the development of computational methods for analyzing the transonic flow about isolated wings and simple wing-body combinations. At the present time, a number of methods are readily available and widely used in this country.[2-7] These methods differ from one another in the complexity of the governing equations and boundary conditions, computational grids, finite-difference schemes, and solution algorithms. Consequently, the solution accuracy and computation times of these codes vary considerably, depending upon the particular geometry and flight conditions.

The problem, then, that faces the aerodynamicist is—which method to use? Since additional complexities result in increased costs of solutions, clearly the simplest method which yields satisfactorily accurate results for the problem at hand should be used.

Presented as Paper 80-0003 at the AIAA 18th Aerospace Sciences Meeting, Pasadena, Calif., Jan. 14-16, 1980; submitted Sept. 29, 1980; revision received March 24, 1981.

*Specialist Engineer.
†Scientist.

The accuracies and computational efficiencies of current methods can best be determined by a systematic comparison with reliable experimental data. Most of the transonic test data which are available are unsuitable for inviscid transonic code correlation because of one or more factors such as low test Reynolds number, old technology wing design, wind tunnel wall interference, limited pressure data, or complex wing-body geometries which cannot be properly modeled in the codes. There is, therefore, a need for new, reliable transonic data for code correlation.

To alleviate the above situation, a comprehensive research program was initiated in 1978 to 1) acquire a set of quality, correlation-tailored, transonic test data for a series of isolated advanced technology wings and simple wing-body combinations which would serve as a standard for future method evaluations, and 2) utilize these data to initiate the evaluation of selected three-dimensional transonic codes.

This paper summarizes the program with particular emphasis on evaluation of the 3-D transonic wing codes. Details of the program are contained in Ref. 8.

Wing Design

The following philosophy was adopted in this program with regard to wing design.

1) Proven design techniques were used to obtain wings with modern aft-loaded airfoils which are not necessarily optimized, but which produce well-behaved flowfields.

2) Wings were used which are geometrically simple. This not only simplifies the task of applying surface boundary conditions in the computational methods, but also makes test model fabrication easier.

3) A range of wing sweeps and aspect ratios was covered which is representative of transport and fighter aircraft.

The planform shapes for the correlation wings are shown in Fig. 1 and the overall geometric characteristics are summarized in Table 1. The configurations are referred to as Wings A, B, and C. Wing A is representative of an advanced transport concept while Wings B and C are characteristic of fighter-type aircraft. Together these wings provide a good range of aspect ratios (from 2.6 to 8.0) and sweep angles (from 25 to 40 deg) for code correlations. Details of the aerodynamic design process can be found in Ref. 8.

Apparatus

Models

Semispan (reflection-plane) models of the wings were fabricated for testing as isolated wings and as wing-fuselage combinations. The fuselage used in these tests was a simple shape, having an elliptical forebody and afterbody with a

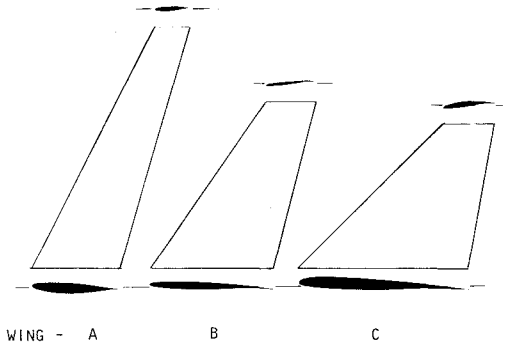

Fig. 1 Planform of correlation wings.

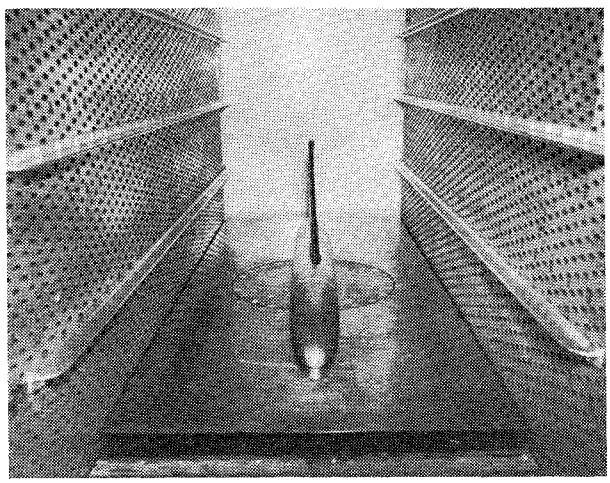

Fig. 2 Test apparatus.

constant section in the wing region. Three different fuselage center-sections were required for each wing to allow testing in high-, mid-, and low-wing positions.

Test Facility

The semispan models were tested in the Lockheed-Georgia Compressible Flow Wind Tunnel (CFWT). The CFWT is a blow-down wind tunnel capable of Reynolds numbers up to 180 million/m (55 million/ft). The test section is 50.8 cm (20.0 in.) wide by 71.2 cm (28.0 in.) high. The top and side walls of the three-dimensional test section have variable porosity capability (from 0 to 10%). The bottom wall, where the model is mounted, is solid. The model is mounted on a five-component balance located in the floor. The wind-tunnel floor boundary layer is removed by a bleed duct located 53.6 cm (21 in.) ahead of the balance centerline. The main features of the test apparatus are illustrated in the photograph of Fig. 2.

Instrumentation

Instrumentation for this test program consists of a five-component strain gage balance to measure model aerodynamic forces. One hundred and sixty surface pressure taps were installed in the wing at five spanwise stations. Six pressure rails, each containing 31 static pressure taps, were mounted on the tunnel walls as shown in Fig. 2. The far-field measurements were extended to the symmetry plane by a streamwise row of fourteen pressure taps along the tunnel floor on each side of the model.

Tests and Methods

Test Conditions

The three wings were tested over a wide range of conditions to provide data at off-design as well as design conditions. The test Reynolds number based on mean aerodynamic chord was nominally six million for Wing A and ten million for Wings B and C. Transition strips were applied to both the upper and lower surface at a fixed distance from the leading edge equal to 5% of the mean aerodynamic chord.

Table 1 Wing model geometry

	Wing		
	A	B	C
AR	8.0	3.8	2.6
λ	0.4	0.4	0.3
$\Lambda_{c/4}$, deg	25.0	30.0	38.4
θ_r, deg	2.76	2.50	2.38
θ_t, deg	−2.04	−4.00	−5.79
$(t/c)_r$, %	12.0	6.0	7.0
$(t/c)_t$, %	12.0	6.0	11.0
$S/2$, cm^2	528.0	530.0	523.0
$b/2$, cm	45.7	31.8	26.1
C_r, cm	16.51	23.88	30.83
C_t, cm	6.60	9.55	9.25

The angle of attack and tunnel Mach number were varied over a wide range: from zero-lift to above design values, and speeds from subcritical through drag-rise Mach number, respectively.

Most of the wind tunnel testing was conducted at a fixed wall porosity of 4% because previous tests in the CFWT had indicated this value would provide minimum wall interference effects. However, in order to properly assess the effect of wind-tunnel wall interference, each of the wings was tested over a range of wall porosities varying from 3 to 6%.

Test Techniques

Since the primary objective of this program was to establish a set of benchmark data suitable for evaluations of theoretical codes, considerable effort was expended to evaluate those aspects of the test techniques which could affect the quality of the results. Of particular note were the evaluation of the wind tunnel boundary layer removal system and calibration of the new wind-tunnel test section configuration. These tests showed the bleed system to be effective in removing the upstream tunnel-floor boundary layer, thus ensuring good reflection-plane characteristics for the semispan wings. Furthermore, the flow in the test section was found to be uniform under these conditions.

Wind Tunnel Wall Interference

Transonic wind tunnel experiments are generally plagued by interference effects from the tunnel walls. These wall-induced effects can be very large and without proper evaluation can result in uncertainty in the quality of the data. If the test data are to be used to correlate theoretical methods, as in the present investigation, the effects of transonic wall interference must be taken into account in the correlations. Only in this way can the adequacy of the mathematical models used in the theoretical methods be properly evaluated.

Conventional Methods

Conventional linear correction methods for treating wind-tunnel wall interference effects at transonic speeds have been found to be generally inadequate. Nonlinear methods are currently under development,[9-11] but these procedures are still in an embryonic state, and generally are rather restrictive. A major weakness in these methods (linear and nonlinear) is the use of the classical homogeneous wind-tunnel wall boundary condition. This model is a simplified linear approximation of a complex viscous-flow process. Consequently, methods employing this model have been useful only in providing qualitative estimates of wind tunnel wall interference.

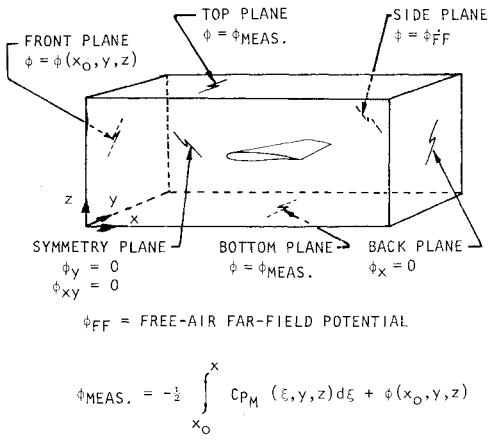

Fig. 3 Boundary conditions for wind-tunnel simulation.

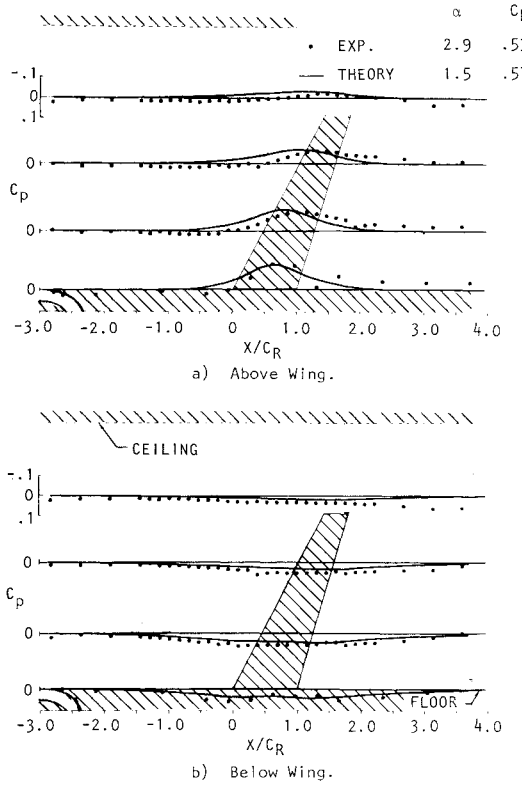

Fig. 4 Comparison of measured and theoretical free-air pressures near the tunnel wall for Wing A at $M = 0.82$.

Development of New Method

A simple, but rigorous, concept for eliminating wind-tunnel wall effects from code correlations is to measure flow-field properties on control surfaces near the tunnel walls during the experiments and to introduce the measured values directly into the computational method as outer boundary conditions.[12,13] This procedure eliminates the need for a theoretical model for the wall boundary condition, and thus ensures that the true nonlinear character of the porous walls are properly taken into account. A comparison of calculated and measured flow properties at the model surface then serves to identify deficiencies (rotation, viscosity, numerics, etc.) in the computational code. Furthermore, a comparison of calculations based on free-air far-field boundary conditions and those based on measured outer boundary conditions serves to give a precise, quantitative assessment of the wind tunnel wall interference.

The formulation of a procedure for incorporating measured boundary conditions in a finite-difference code is illustrated in Fig. 3. A rectangular computational boundary is established around the wing, with the top, bottom, and side planes approximating the locations of the porous wind tunnel walls. The boundary conditions near the upper and lower walls are determined by integrating measured static pressure distributions as illustrated. The wall-induced velocity perturbations on the side plane are assumed to be sufficiently small such that the disturbance potential can be approximated by an asymptotic far-field solution.[14] At the downstream boundary, $\phi_x = 0$ is assumed. The usual symmetry conditions, $\phi_y = \phi_{xy} = 0$, are applied on the plane of symmetry.

The perturbation potential at the upstream boundary, $\phi(x_0, y, z)$, requires special treatment. If the flow-inclination angles are expressed as combinations of the free-air values and wall-induced perturbations to the free-air values, then it can be shown that

$$\phi(x_0, y, z) = \phi_{FF}(x_0, y, z) + \int_{z_0}^{z} \delta\alpha(x_0, y_0, \zeta)\, d\zeta + \int_{y_0}^{y} \delta\beta(x_0, \eta, z)\, d\eta \tag{1}$$

where α and β are the upflow and crossflow inclination angles, respectively. These wall-induced upwash and crossflow distributions at the upstream boundary, $\delta\alpha$ and $\delta\beta$, represent the lift interference contributions, and their effect is approximately equivalent to that produced by a change in angle of attack or sideslip in a free-air solution. Therefore the approach used herein is to ignore the sideslip correction, $\delta\beta$, and to approximate the $\delta\alpha$ integral by a simple adjustment in the angle of attack. The angle-of-attack correction, $\Delta\alpha$, is found by matching computed and measured pressures in the leading edge region of the wing where the pressures are very sensitive to angle of attack.

Application of New Method

The incorporation of measured outer boundary conditions in each of the evaluated transonic codes was outside the scope of this research program. The technique was applied, however, to one of the selected codes in order to 1) verify the formulated procedure, and 2) provide at least an approximate assessment of, and correction for, wall interference effects in the correlations performed herein. The extended small disturbance transonic code of Bailey and Ballhaus[2] was chosen for convenience. The finite Cartesian grid used therein makes the code ideally suited for inclusion of experimentally-derived outer Dirichlet boundary conditions.

A comparison of theoretical free-air[2] and measured pressure distributions on the control surfaces above and below Wing A is presented in Fig. 4. The comparison is presented at the wing design condition using angles of attack which have been adjusted to give approximately the same lift coefficient. Differences in the measured wind-tunnel pressures and the computed free-air pressures are relatively small, indicating that the wall-induced interference effects are small in this case.

When the experimental far-field pressures (Fig. 4) are incorporated as boundary conditions in the transonic code, the typical effect on the computed surface pressures for Wing A is as shown in Fig. 5. The broken line corresponds to the free-air conditions noted in Fig. 4, while the dashed line is the result of specifying experimental far-field pressures. At these conditions the wall interference effects are small, resulting in a forward shift in the shock location of approximately 5% chord and a general depression of the upper surface suction level.

Having quantified the typical influence of the wind tunnel walls, an investigation was made to determine if the interference effects were "correctable." That is, if a range of flow conditions existed whereby the wind tunnel wall in-

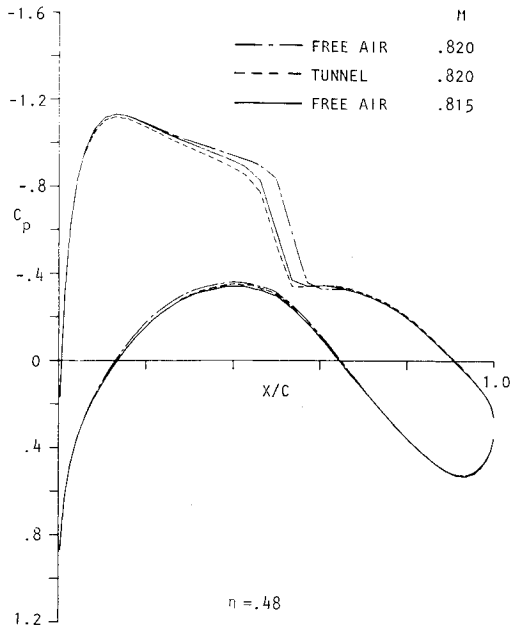

Fig. 5 Theoretical pressure distributions for Wing A using free-air and measured tunnel boundary conditions; $\alpha = 1.5$ deg.

terference effects could be treated by a simple adjustment in freestream Mach number and angle of attack. The theoretical free-air solution was recomputed while varying freestream conditions to obtain the best possible match with computed wing pressures using measured boundary conditions. Figure 5, which is representative of results for the complete wing, shows that wing pressures computed with a simple correction to freestream Mach number of approximately $\Delta M = -0.005$ closely agree with computations based on the measured boundary conditions at the test Mach number. A similar result would be expected from a full potential solution. The wall induced perturbations are small (Fig. 4), justifying the small-disturbance formulation.

Thus, for Wing A, the test data obtained in the wind-tunnel at the conditions noted can be reinterpreted to free-air conditions at a corrected Mach number which is approximately 0.005 less than the wind tunnel test Mach number. Similar analyses were conducted for Wings B and C. Again, it was found that a small constant adjustment of $\Delta M = -0.005$ was sufficient to remove the effect of blockage interference from the test data, at the design conditions for the wings.

These analyses will have to be repeated at other test conditions of interest. The blockage correction for a given wing will vary with Mach number, lift coefficient, and wind-tunnel wall porosity. Furthermore, there may be test conditions for which the interference effects are not correctable by simple Mach number adjustments. The only recourse in these instances will be to incorporate the measured boundary conditions directly into the code being evaluated.

Computational Methods

The three-dimensional transonic computational methods selected for evaluation in this program are 1) the Bailey-Ballhaus code,[2] 2) the Jameson-Caughey FLO-22 code,[5] and 3) the Jameson-Caughey FLO-27 code.[7] Salient features of each code are discussed briefly.

Bailey-Ballhaus Code

The Bailey-Ballhaus code solves a modified or extended small disturbance (ESD) approximation of the full potential equation. Linearized wing boundary conditions are applied in the wing reference plane. The embedded grid scheme of Boppe[3] is followed in which a fine skewed inner grid (enclosing the wing) is embedded within a crude Cartesian outer grid. The outer computational grid is finite with boundary conditions given by the Klunker asymptotic far-field expansion.[14] The program is formulated using both nonconservative and fully conservative differencing. The desired form is a user option.

FLO-22 Code

The Jameson-Caughey FLO-22 program is a production code capable of treating the flow about yawed or swept wings. The method solves a quasilinear (nonconservative) form of the full potential equation (FPE) which has been explicitly transformed to a boundary conforming coordinate system. The coordinate system is generated by a sequence of numerical shearing transformations, and a square-root mapping about a point inside the wing leading edge. This results in a desirable concentration of grid points in the nose region, but the simple shearing, however, results in a spanwise decrease in the number of grid points on the wing.

FLO-27 Code

The Jameson-Caughey FLO-27 program is a pilot code capable of treating the flow about an isolated yawed or swept wing, or one mounted on an infinite circular cylinder. A finite-volume scheme is used to difference the full potential equation in conservative form. The analysis of FLO-27 is based on a numerical calculation of the required transformation derivatives at each grid point in the computational region. Thus, in principle, the method can be adapted to treat configurations of arbitrary geometric complexity simply by providing the Cartesian coordinates of each mesh point. This flexibility is achieved at the expense of an increase in computation time and some loss in accuracy because the transformation coefficients must be calculated numerically for each relaxation cycle.

In the present version of the program, the computational grid is generated by a sequence of global mappings which are similar to those used explicitly in FLO-22. The main difference (for isolated wings) is that in FLO-27 the wing chord is covered by the same number of grid points at every span station.

Code Correlations

In this section experimental wing-alone pressures are compared with theoretical solutions. First, nonconservative relaxation (NCR) inviscid solutions generated using FLO-22 and the Bailey-Ballhaus code are compared with experimental data. Next, fully conservative relaxation (FCR) inviscid results computed using FLO-27 and the Bailey-Ballhaus code are correlated. Finally, viscous effects are assessed from results obtained using the FLO-22 code iteratively coupled with a two-dimensional turbulent boundary layer method.[15]

Solution convergence for each code was established from an examination of the time-history of the wing pressure distributions. Typical CDC 7600 computing times were 6, 15, and 30 min for the ESD, FLO-22, and FLO-27 codes, respectively. Grid features, computing efficiencies, and code convergence characteristics are detailed in Ref. 8.

All calculations were made for isolated wings in free-air conditions using Mach numbers and angles of attack corrected according to the technique described earlier. Since the small disturbance approximation is invalid in the wing leading-edge region, the full potential solution (FLO-22) was used to establish the corrected α.

Wing A—High Aspect Ratio, Low Sweep

Computed Wing A inviscid nonconservative FPE and ESD solutions are compared with experiment in Fig. 6. The agreement between FPE and experiment is surprisingly good in view of the fact that the boundary layer was neglected in the calculations. The only serious discrepancies between theory and experiment are in the aft portion of the wing where the calculations overpredict the loading.

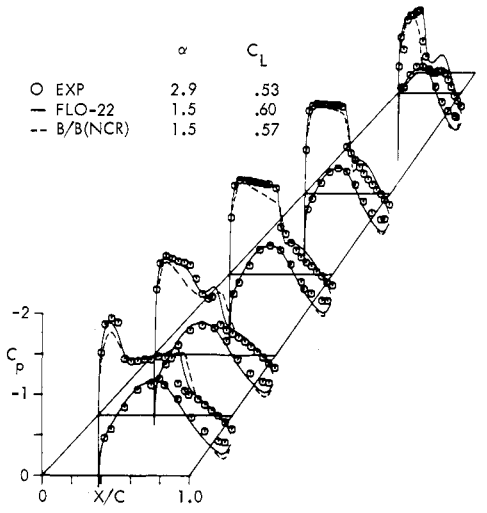

Fig. 6 Comparison of nonconservative solutions with experiment for Wing A at $M = 0.82$.

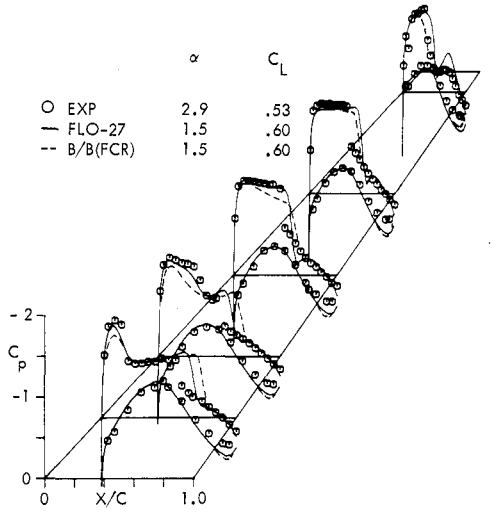

Fig. 7 Comparison of conservative solutions with experiment for Wing A at $M = 0.82$.

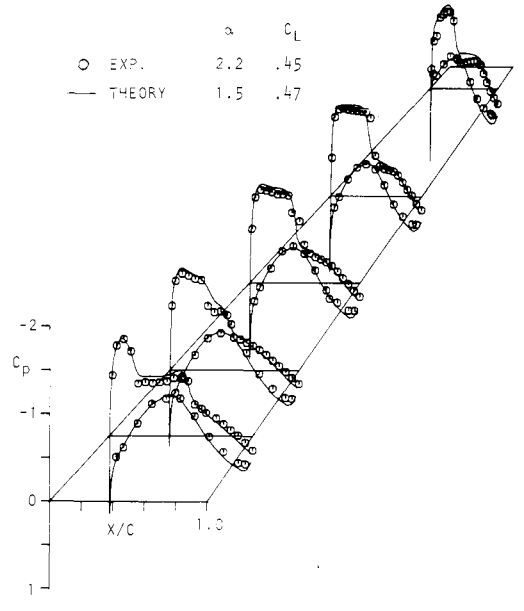

Fig. 8 Comparison of FLO-22 results with experiment when viscous corrections are included; Wing A, $M = 0.82$.

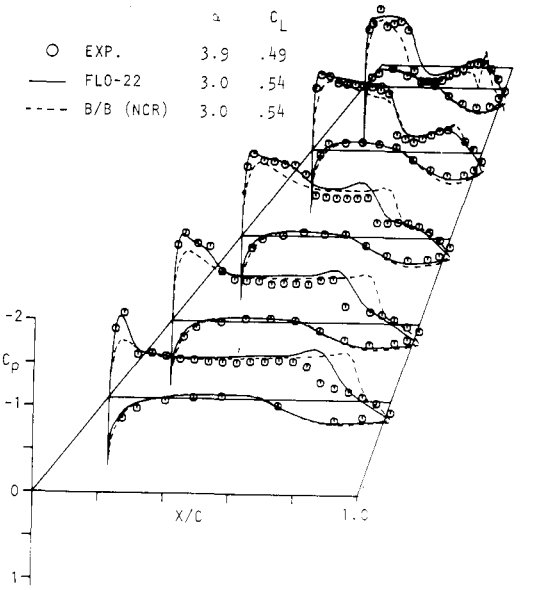

Fig. 9 Comparison of nonconservative solutions with experiment for Wing B at $M = 0.90$.

The small-disturbance results also are in good agreement with experiment, but not as good as the full potential solution. The ESD results overpredict the airfoil aft loading to about the same extent as did the full potential calculations. However, unlike the full potential results, the ESD solution misses the weak (supersonic to supersonic) oblique leading-edge shock and mispredicts the plateau pressure gradient upstream of the outboard shock wave. The failure to properly capture the leading edge shock is characteristic of small disturbance formulations and primarily due to the relatively large shock sweep.

Using the angle of attack selected from the full potential nonconservative correlations, fully conservative solutions were generated using the FLO-27 and Bailey-Ballhaus codes. Comparisons with experiment are summarized in Fig. 7. Comparison of these results with the nonconservative solutions shown in Fig. 6 shows that fully conservative solutions result in the expected aft shift in shock location from the NCR shock position and an increase in strength. Otherwise, the fully conservative solutions are very similar to nonconservative results.

In order to assess the magnitude of viscous effects, calculations were performed with viscous displacement-surface effects included in the full potential NCR solution. The angle of attack was again adjusted to match experimental and calculated pressures in the nose region. The viscous calculations are compared with experiment in Fig. 8. These data show that full potential NCR calculations using an iterated 2-D boundary layer result in excellent agreement with experiment. Not only are the shock waves properly computed, but the aft loading is correctly predicted. Thus the inclusion of a simple strip boundary layer within the calculations improves the agreement between measured and computed lift over that resulting from inviscid solutions.

Wing B—Moderate Aspect Ratio and Sweep

Both FPE and ESD nonconservative solutions are compared with experimental data for Wing B in Fig. 9. Here, the good agreement between FLO-22 solutions and experiment is evident, as is the relatively poor agreement between ESD results and experiment. The ESD method fails to capture the weak leading edge shock, and positions the trailing edge shock too far aft at the wing root. The spurious ESD tip pressures are probably attributable to the lack of coarse grid resolution at the tip. This is a fundamental problem with the grid embedding scheme.

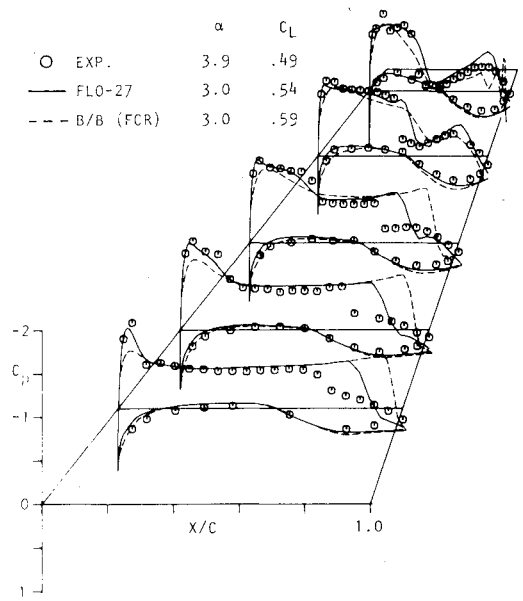

Fig. 10 Comparison of conservative solutions with experiment for Wing B at $M = 0.90$.

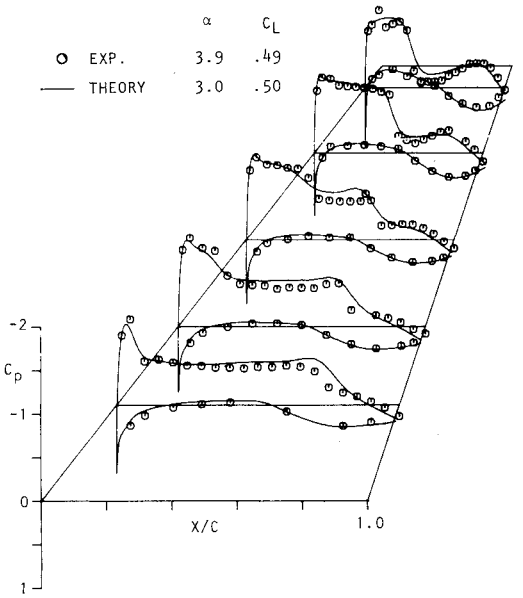

Fig. 11 Comparison of FLO-22 results with experiment when viscous corrections are included; Wing B, $M = 0.90$.

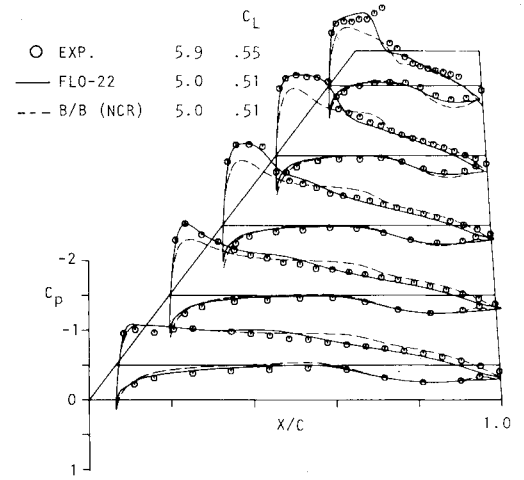

Fig. 12 Comparison of nonconservative solutions with experiment for Wing C at $M = 0.85$.

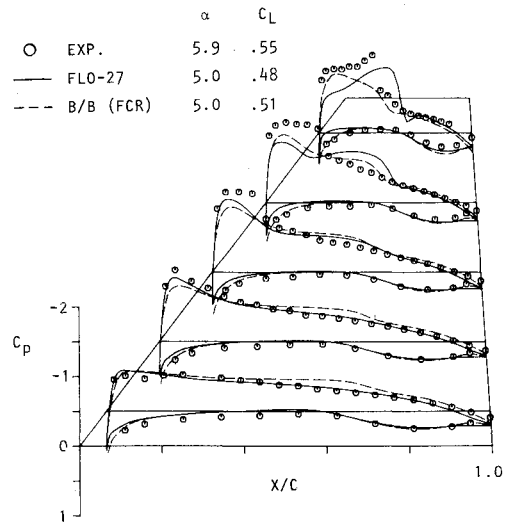

Fig. 13 Comparison of conservative solutions with experiment for Wing C at $M = 0.85$.

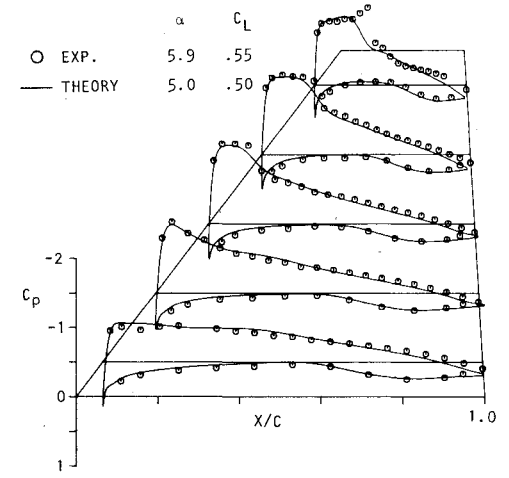

Fig. 14 Comparison of FLO-22 results with experiment when viscous corrections are included; Wing C, $M = 0.85$.

A calculation was performed to investigate the sensitivity of the ESD solution to grid density in the leading edge region, with the aim of improving the shock capture characteristics. The number of grid points in the forward 10% chord was doubled from the default value of 7 per surface to 14. The resulting calculation did show a modest increase in the leading edge suction peak, but the "shock" was still badly smeared—to the point of being almost indiscernible.

Figure 10 contains the comparisons of FPE and ESD conservative solutions with Wing B experimental data. The use of fully conservative differencing causes a degradation in the correlations as evidenced by a comparison of Figs. 9 and 10. The degradation is primarily manifested in the too-far aft positioning of the shock wave in the conservative calculations.

The inclusion of a boundary layer in the FLO-22 solution process produces excellent agreement between theory and experiment shown in Fig. 11. The excessive smearing of the computed leading edge shock wave might be avoided by the use of a more closely spaced grid. Of note in these results is the good prediction of aft loading, and the close agreement between predicted and measured lift.

Wing C—Low Aspect Ratio, High Sweep

Figure 12 compares FPE and ESD nonconservative solutions with Wing C experimental data. Although the correlation is not quite as good as it was for Wings A and B,

FLO-22 solutions are in fair agreement with experiment. The major differences between theory and experiment occur near the tip and may be due to vortex roll-up which is not modeled in the theory. On the other hand, the ESD solution is a poor representation of experiment. This failure is really not surprising because as wing sweep increases, some of the nonlinear cross-flow terms which were neglected in the formulation become important.

Fully conservative relaxation does not improve the agreement between theory and experiment for Wing C, as evidenced by Fig. 13. In this case, FCR actually caused a deterioration of the quality of the full potential results, and did nothing to improve the extended small disturbance.

The inclusion of viscous effects in the FLO-22 calculation (Fig. 14) results in only marginal improvement in the correlation (cf. Figs. 12 and 14). In fact, the effect of viscosity (within the framework of a displacement surface concept) is very small, as evidenced by the slight 0.01 decrease in lift coefficient at the fixed angle of attack. Almost all of the lift lost is attributable to the forward movement and slightly increased smearing of the shock.

Conclusions

A comprehensive program was formulated and conducted for the specific purpose of acquiring test data suitable for current and future three-dimensional transonic code correlations. High-quality test data were obtained for three advanced technology wings by using a unique test apparatus and by devoting careful attention to details of the experiment. The data have been used in preliminary evaluations of three selected transonic computational methods. The following salient conclusions can be drawn from this research.

1) The measurement of far-field pressures provides a means for assessing transonic wind tunnel wall interference effects without assumptions concerning the nature of the flow through the porous walls.

2) For a range of test conditions the wind tunnel data obtained herein can be corrected to equivalent free-air conditions by small adjustments in Mach number and angle of attack.

3) Full potential solutions are uniformly in better agreement with experiment than small disturbance results.

4) Nonconservative formulations more closely predicted measured pressures than conservative formulations.

5) For both full potential and extended small disturbance solutions the correlation deteriorates as wing sweep increases and aspect ratio decreases. However, the degradation is much worse for the extended small disturbance code.

6) Extended small disturbance results can be considered adequate only for the high aspect ratio, moderately swept wing.

7) A two-dimensional boundary layer analysis provides an adequate representation of viscous effects for wings operating at cruise conditions where shock waves are weak.

Acknowledgments

The results reported are based on research partially supported by the Air Force Office of Scientific Research (ASFC), United States Air Force, under Contract No. F49620-78-C-0068. The United States Government is authorized to reproduce and distribute reprints for governmental purposes notwithstanding any copyright notation hereon.

References

[1] Ballhaus, W.F. and Bailey, F.R., "Numerical Calculation of Transonic Flow About Swept Wings," AIAA Paper 72-677, June 1972.

[2] Ballhaus, W.F., Bailey, F.R., and Frick, J., "Improved Computational Treatment of Transonic Flow About Swept Wings," NASA CP-2001, Nov. 1976.

[3] Boppe, C.W., "Calculation of Transonic Wing Flows by Grid Embedding," AIAA Paper 77-207, Jan. 1977.

[4] Boppe, C.W., "Computational Transonic Flow About Realistic Aircraft Configurations," AIAA Paper 78-104, Jan. 1978.

[5] Jameson, A. and Caughey, D.A., "Numerical Calculation of the Transonic Flow Past a Swept Wing," C00-3077-140, ERDA Mathematics and Computer Laboratory, New York Univ., June 1977 (also available as NASA CR-153297).

[6] Caughey, D.A. and Jameson, A., "Numerical Calculation of Transonic Potential Flow About Wing Fuselage Combinations," AIAA Paper 77-677, June 1977.

[7] Jameson, A. and Caughey, D.A., "A Finite Volume Method for Transonic Potential Flow Calculations," AIAA Paper 77-635, June 1977.

[8] Hinson, B.L. and Burdges, K.P., "Acquisition and Application of Transonic Wing and Far-Field Test Data for Three-Dimensional Computational Method Evaluation," AFOSR-TR-80-0421, March 1980.

[9] Chan, Y.Y., "A Perturbation Theory of Two-Dimensional Transonic Wind Tunnel Wall Interference," NAE LR-598, April 1978.

[10] Murman, E.M., "Computation of Wall Effects in Ventilated Transonic Wind Tunnels" AIAA Paper 72-1077, Sept. 1972.

[11] Shankar, V., Malmuth, N.D., and Cole, J. D., "Computational Transonic Design Procedure for Three-Dimensional Wings and Wing-Body Combinations," AIAA Paper 79-0344, Jan. 1979.

[12] Kemp, W.B. Jr., "Transonic Assessment of Two-Dimensional Wind Tunnel Wall Interference Using Measured Wall Pressures," NASA CP-2045, Part 2, March 1979.

[13] Stahara, S.S. and Spreiter, J.R., "A Transonic Wind Tunnel Interference Assessment—Axisymmetric Flows," AIAA Paper 79-0208, Jan. 1979.

[14] Klunker, E.B., "Contribution of Methods for Calculating the Flow About Thin Lifting Wings at Transonic Speeds—Analytical Expressions for the Far-Field," NASA TN D-6530, 1971.

[15] Nash, J.F. and Macdonald, A.G.J., "The Calculation of Momentum Thickness in a Turbulent Boundary Layer at Mach Numbers up to Unity," Aeronautical Research Council, C.P. 963, 1967.